UNIVERSITY OF TORONTO

Modelling of d-wave Tunnelling Devices and Proximity Tunnelling Devices

by

Jianwei Xu

A thesis submitted in partial fulfillment for the
degree of Master of Science

in the
Faculty of Arts & Science
Department of Physics

August 2012

UNIVERSITY OF TORONTO

Abstract

Faculty of Arts & Science
Department of Physics

Master of Science

by Jianwei Xu

In this thesis the calculation of tunnelling spectroscopy based on BTK is discussed, which is extended to model the devices of our new results. Also, we are interested in establishing a method of calculating the spectroscopy taking into account proximity effect.

Acknowledgements

Thanks for the priceless help from my supervisor, Prof. Ken Burch, and all the people who helped me...

Contents

Chapter 1

Introduction

Tunnelling spectroscopy of superconductors is a heavily studied topic. The typical experimental results are modelled based on the work of BTK[1] which is a simple theory for the I-V curve of normal superconducting junction including calculating the tunnelling spectroscopy based on the use of Bogoliubov equations. Extension of the theory, however, should be explored as in BTK, the calculation of tunnelling spectroscopy is for simple s-wave case, and the assumed step function of pair potential should be questioned , additionally, there are newly conducted experiments, showing some new features of the tunnelling spectroscopy[2–4].

In consequence, one extension of the BTK theory discussed by various authors[5–7] is to establish theory of the d-wave tunnelling spectroscopy, which is required by various experiments[8, 9]. Another more basically approach is to include the proximity effect, where we need to refer to Bogoliubov equations[3, 10, 11]. Moreover, our group has a featured publication containing the topic of proximity effect. To more fully illustrate the experimental results in our group, it is necessary to establish a d-wave tunnelling spectroscopy theory accounting for proximity effect, which hasn't been clearly discussed before. Currently our work is in progress.

Chapter 2

Tunnelling Spectroscopy of D-Wave Superconductors

2.1 Properties of Energy Gaps

The Hamiltonian of the interaction in superconductor is defined as

$$H_{eff} = \sum_{k,k'} V(\mathbf{k},\mathbf{k}') C^{+}_{k'} C^{+}_{-k'} C_{-k} C_{k} \tag{2.1}$$

where $V(\mathbf{k},\mathbf{k}')$ represents interaction, $C^{+}_{k'}$ creator of k' cooper pair, and C_k annihilator of k cooper pair. The pair potential is defined as

$$\Delta(k) = -\sum_{k'} V(\mathbf{k},\mathbf{k}') < C_{-k'} C_{k'} > \tag{2.2}$$

The key difference between isotropic superconductor and anisotropic superconductor is their $\mathbf{k}$ space dependence of potential, V. In isotropic superconductors, potential is chosen as an averaged value independent of $\mathbf{k}$ space, resulting the independence of $\mathbf{k}$ space of pair potential.

2.1.1 Some Conclusions of BCS Theory

The superconductor of the BCS theory is assumed to be isotropic[12], so that,

$$\Delta = -V \sum_{k'} < C_{-k'} C_{k'} > \tag{2.3}$$

Based on this assumption, they conclude that

$$\frac{1}{N(0)} = \int_0^{\hbar\omega} \frac{d\epsilon}{\epsilon^2 + \Delta^2} \tanh\left[\frac{1}{2}\beta(\epsilon^2 + \Delta^2)^{\frac{1}{2}}\right], \beta = \frac{1}{kT} \tag{2.4}$$

when near T_c, (2.4) has a simple expression

$$\Delta = 3.2kT_c(1 - \frac{T}{T_c})^{\frac{1}{2}} \tag{2.5}$$

2.1.2 ~~Electric Properties of~~ Pair Potential of Anisotropic Superconductors

When dealing with anisotropic superconductors, the interaction is no longer $\mathbf{k}$ space independent, leading to the fact that we have to change the form of pair potential. Assuming that the interaction is only determined by the angle between $\mathbf{k}, \mathbf{k}'$ and expand the interaction accordingly.

$$V_{kk'} = V(\mathbf{k} \cdot \mathbf{k}') = V(\cos\theta_{kk'}) = \sum_l (2l+1) V_l P_l(\cos\theta_{kk'}) \tag{2.6}$$

where P_l represent Legendre Functions, in which

$$V_l = \frac{1}{2} \int_{FS} \frac{d\Omega}{4\pi} V_{kk'} P_l(\cos\theta_{kk'}) \tag{2.7}$$

Notice that the integral is limited to fermi surface. Using Green function method we could derive that

$$\Delta(\widehat{\mathbf{k}}, T) = \Delta_a(T)\sqrt{4\pi} Y_{lm}(\theta_k, \phi_k) \tag{2.8}$$

where Y_{lm} are spherical harmonics. The average $\Delta_a(T)$ over $\mathbf{k}$ satisfies

$$1 = \frac{1}{2}|V_l| \sum_{k'} \frac{4\pi |Y_{lm}(\widehat{k'})|^2 \tanh(\frac{1}{2}\beta\epsilon_{k'})}{\epsilon_{k'}} \tag{2.9}$$

where

$$\Delta_{k'} = \sqrt{\epsilon_{k'}^2 + 4\pi\Delta_a^2(T)|Y_{lm}(\widehat{\mathbf{k}})|^2} \tag{2.10}$$

Similar to BCS theory, we replace the sum operator with integral

$$\sum_k = \int d\Omega \int_0^{\hbar\omega} d\epsilon = \int_0^{2\pi} d\phi \int_0^{\pi} \sin\theta d\theta \int_0^{\hbar\omega} d\epsilon \tag{2.11}$$

We could get the equation

$$1 = N(0)|V_L| \int d\Omega \int_0^{\hbar\omega} d\epsilon \frac{4\pi |Y_{lm}(\theta,\phi)|^2 \tanh(\frac{1}{2}\beta\epsilon)}{\epsilon} \tag{2.12}$$

2.1.3 Energy Gap Terms Selected for the Calculation

If we fix the temperature, only the formal solution(2.8) is used, in which we treat term $\Delta_a(T)$ as a constant. Therefore, for s-wave,

$$\Delta = \Delta_a(T)\sqrt{4\pi}Y_{00}(\theta_k,\phi_k) = \Delta_a(T)\sqrt{4\pi}\cdot\frac{1}{2}\sqrt{\frac{1}{\pi}} \sim \Delta_0 \tag{2.13}$$

and for d-wave we limit to $d_{x^2-y^2}$, we have,

$$\Delta \sim \Delta_0(\widehat{k}_x^2 - \widehat{k}_y^2) \sim \Delta_0 \cos(2\phi), \phi = \arctan(\widehat{k_x}/\widehat{k}_y) \tag{2.14}$$

Their shapes are like

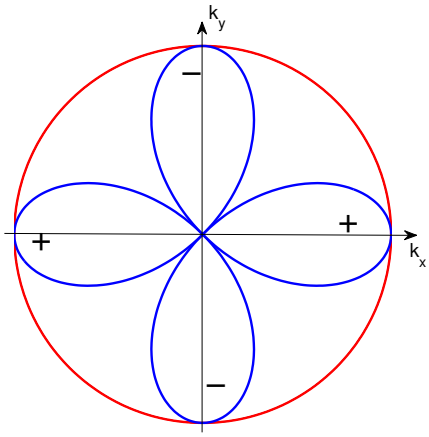

FIGURE 2.1: The shape of s-wave energy gap is a circle while that of d-wave energy gap is like a petal. Notice that the $d_{x^2-y^2}$ has two positive and negative leaves

2.2 *D*-Wave Tunnelling Spectroscopy of Superconductors

To approach the calculation of tunnelling spectroscopy of superconductors to fit the experimental results in our group, there are several steps to go in both theory and calculation. First of all, we need to establish the model for s-wave, the basis for the following calculations. Second, with the s-wave model established, replacing the term

(2.22) with (2.23) when conducting the integral will guide us to the d-wave tunnelling spectroscopy results. Finally, we obtain the conductances that can be compared to our BSCCO on BSC experiments. Additionally, algorithm for fitting the results need to be implemented. We, ~~however~~, first ~~of all,~~ introduce the final method of calculating the conductance versus bias[1] before we discuss the details of the d-wave tunnelling spectroscopy.

2.2.1 I-V Curve Function For N-S Boundary

The reference[1] derives that the I-V curve for N-S Boundary could be written like

$$I_{NS} = 2N(0)ev_F\mathcal{A}\int_{-\infty}^{\infty}[f_0(E-eV)-f_0(E)][1+A(E)-B(E)]dE \tag{2.15}$$

in which $f_0(E)$ is the fermi distribution

$$f_0(E) = \frac{1}{1+e^{(E-\mu)/kT}} \tag{2.16}$$

where terms μ is the chemical potential. By applying a differential operation on (2.27) we get that

$$\sigma = \frac{\partial I}{\partial V} = \int_{-\infty}^{\infty}\sigma_T(E)\frac{\partial f_0(E-eV)}{\partial V}dE \tag{2.17}$$

Omitting the constant factor, the following term is what we are focusing on

$$\sigma_T(E) = 1 + A(E) - B(E) \tag{2.18}$$

where $A(E)$ is the famous Andreev reflection and $B(E)$ is the ordinary reflection[1], the former of which reflects a hole and generate a Cooper pair in the superconductor side.

2.2.2 *ab*-Tunnelling Spectroscopy

Since in this chapter we are talking about *d*-wave Tunnelling spectroscopy, there are two cases: *ab* tunnelling in which tunnelling axis is normal to pair potential plain, and *c* tunnelling in which tunnelling axis is parallel to pair potential plain, Fig.2.1. We first of all discuss *ab*-tunnelling spectroscopy. A simple way for the calculation is to assume that the potential is a δ function while energy gap is a step function, Fig.2.2. On this assumption, the Bogoliubov equations have analytical solutions[5]. The positive and negative pair potentials for all cases are defined as

$$\Delta_\pm = |\Delta_\pm|\exp(i\phi_\pm) \tag{2.19}$$

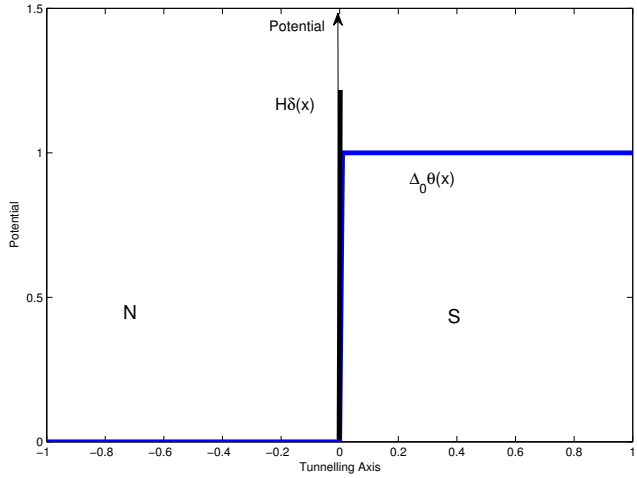

FIGURE 2.2: δ function of potential and step function of energy gap

Following the steps stated before, we write the formula for s-wave case as in the view of tunnelling axis, term (2.19) are step functions.

$$\sigma_R(E) = \frac{\sigma_S(E)}{\sigma_N} = \frac{1 + \sigma_N \mid \Gamma_+ \mid^2 + (\sigma_N - 1) \mid \Gamma_+\Gamma_- \mid^2}{\mid 1 + (\sigma_N - 1)\Gamma_+\Gamma_- \exp(i\phi_- - i\phi_+) \mid^2} \tag{2.20}$$

where the terms $\Gamma_\pm, \sigma_N$ are

$$\Gamma_\pm = \frac{E - \sqrt{E^2 - |\Delta_\pm|^2}}{|\Delta_\pm|}, Z = \frac{Z_0}{\cos\theta}, \sigma_N = \frac{1}{1 + Z^2} \tag{2.21}$$

and we write the term $\sigma_S(E)$ for convenience.

$$\sigma_S(E) = \sigma_N \frac{1 + \sigma_N \mid \Gamma_+ \mid^2 + (\sigma_N - 1) \mid \Gamma_+\Gamma_- \mid^2}{\mid 1 + (\sigma_N - 1)\Gamma_+\Gamma_- \exp(i\phi_- - i\phi_+) \mid^2} \tag{2.22}$$

When we set the phase difference of the two pair potentials zero, $\phi_- - \phi_+ = 0$, the two energy gaps are always the same. Then we get a figure indicating different shapes with different, Z, the barrier hights, in Fig.2.3.

The phase difference between the pair potentials Δ_+ felt by electron like particles and Δ_- felt by hole like particles affects the shape of the s-wave spectroscopy significantly, Fig.2.4.

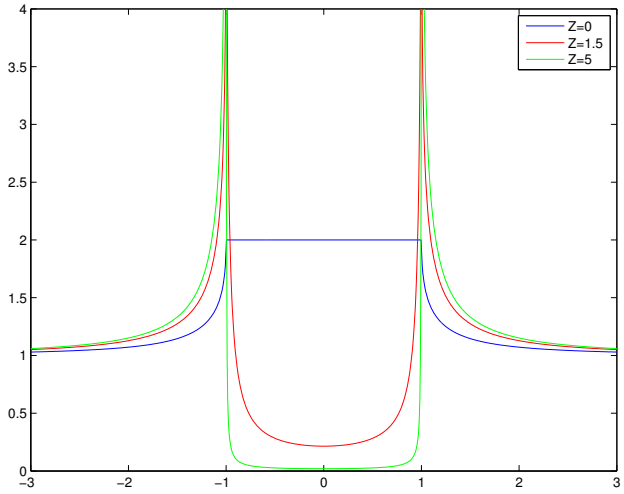

FIGURE 2.3: The picture indicates the different shapes of $\sigma_R(E)$ corresponding to the different barrier values. Here $\Delta_+ = \Delta_-$

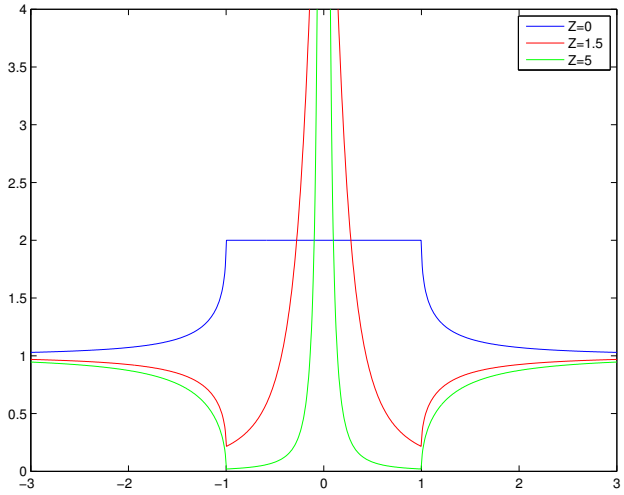

FIGURE 2.4: The picture indicates the different shapes of $\sigma_R(E)$corresponding to the different barrier values. Here $\Delta_+ - \Delta_- = \pi$

Now we move to d-wave case. Here we limit to $d_{x^2+y^2}$ case, in which the positive and negative pair potentials are like

$$\Delta_+ = \Delta_0 \cos 2(\theta - \alpha)$$
$$\Delta_- = \Delta_0 \cos 2(\theta + \alpha) \tag{2.23}$$

In *ab*-tunnelling case, θ represents the incident angle. There phase difference is like

$$e^{i\phi_- - i\phi_+} = \frac{|\Delta_+|}{\Delta_+}\frac{\Delta_-}{|\Delta_-|} = \frac{|\cos 2(\theta-\alpha)|}{\cos 2(\theta-\alpha)}\frac{\cos 2(\theta+\alpha)}{|\cos 2(\theta+\alpha)|} \tag{2.24}$$

Notice that the right term of (2.24) could only be $1, -1$, therefore, if $\alpha \neq 0$, for SOME θ, phase difference is π, for SOME θ, phase difference is 0. The region of θ is determined by α. For instance, if $\alpha = \pi/4$, for all θ, phase difference is π.

The idea is to conduct a solid angel integral after specifying a energy gap term from (2.22) and (2.23), θ in latter of which varies in different cases, that in *ab* tunnelling, φ is the incident angel θ as the petal of the energy gap is in the incident plain, while in *c* tunnelling, θ is the angel in the junction interface.

According to the reference[5], the $\sigma_T(E)$ in (2.28) could be written like

$$\sigma_T(E) = \frac{\int_0^{2\pi} d\varphi \int_{-\frac{\pi}{2}}^{\frac{\pi}{2}} d\theta \sigma_S(E)\cos\theta}{\int_0^{2\pi} d\varphi \int_{-\frac{\pi}{2}}^{\frac{\pi}{2}} d\theta \sigma_N \cos\theta} \tag{2.25}$$

Again similar to $\sigma_R(E)$, the $d_{x^2+y^2}$ is also dependent on the phase difference, which is expressed in (2.24). We show the figure with different α in Fig.2.5.

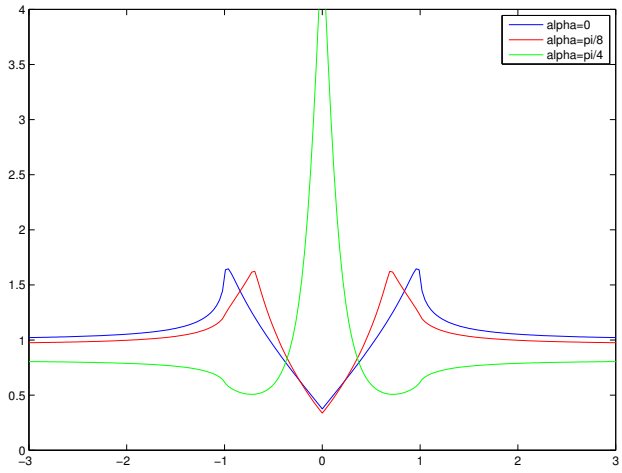

FIGURE 2.5: The figure indicates the correspondence of conductance and angel between incident normal and the petal axis.

Furthermore we limit the phase difference to zero. Figure 2.6 shows the property of the *ab* tunnelling spectroscopy respect to different pair potentials, which indicates that one pair potential corresponds to one peak in the figure, while if pair potential is zero, the tunnelling conductance is a constant, 1.

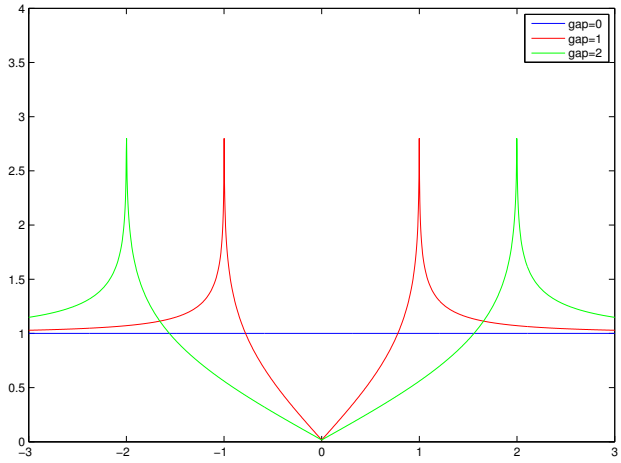

FIGURE 2.6: The figure demonstrates the total tunnelling conductance with different energy gaps. When energy gap amplitude is zero, the peaks vanish, meaning that the material turns into normal metal. Here we choose $Z = 5$

2.2.3 Differential Conductance with Different Temperatures and Fixed Energy Gap Amplitude

In general, the properties of differential conductance is determined by the derivative of the fermi function and tunnelling conductance, according to (2.28) and (2.29). As an illustration,Fig.2.7 shows differential conductance at Temperature 1K, where the top figure is the differential conductance, the bottom figure is the tunnelling conductance, and the others are the derivatives of fermi function at different biases. We see that the peak of the derivatives are close to δ functions, which makes the differential conductance look similar to the tunnelling conductance after the integration.

Let's discuss a way to make the picture more clear in Fig.2.8, demonstrating the relation between the tunnelling conductance with temperature with a FIXED pair potential. We could observe that the dip in middle generally vanish as the temperature increases.

2.2.4 Differential Conductance with Different Pair Potential Amplitudes with Fixed Temperature

Though we should be clearly warned that the energy gap is dependent on the temperature, we still do a study for the relation between differential conductance with energy gap amplitudes.

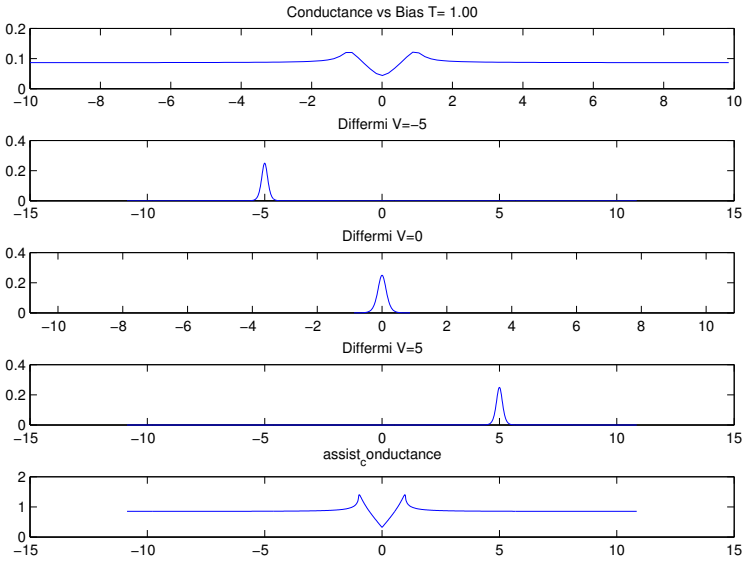

FIGURE 2.7: Differential conductance with T=1K, accompanied by plots of three derivatives of the fermi distributions at varied biases and a tunnelling conductance graph in the bottom.

Generally, the shapes of tunnelling conductance are similar except when the energy gap amplitude is zero, which will make the tunnelling conductance constant, already indicated in Fig.2.6.

Therefore, we simply provide an illustration figure. We could notice that with the increase energy gap amplitude, the centre dip becomes deeper, Fig.2.9.

Now we briefly introduce the calculation methods. It should be learned that we are trying to calculate a second order integral, which may lead a large calculation mission amount, as ~~that~~ we might have to calculate 1000×1000 volume. I developed a simple method based on the essential features of function σ_T and differential fermi distribution function $\frac{\partial f_0(E-eV)}{\partial V}$ in the integration(2.17).

First of all, the function $\sigma_T(E)$ is assumed to be CONSTANT when parameter E's absolute value is "much" large that amplitude of the energy gap, Fig.2.6.

Second, we are acknowledged that differential fermi distribution function is actually of Delta function type, which means the value could be assumed zero when its parameter $E - \mu - eV$ is "much" larger than kT. Also, all the derivatives of the fermi distribution function shares the exact shape, shown in Fig.2.7; their only difference is that the peaks are in different positions corresponding to the value of bias.

We the above knowledge, we calculate the the tunnelling spectroscopy point values according to a chosen step length ONLY ONCE and store the data. When parameter

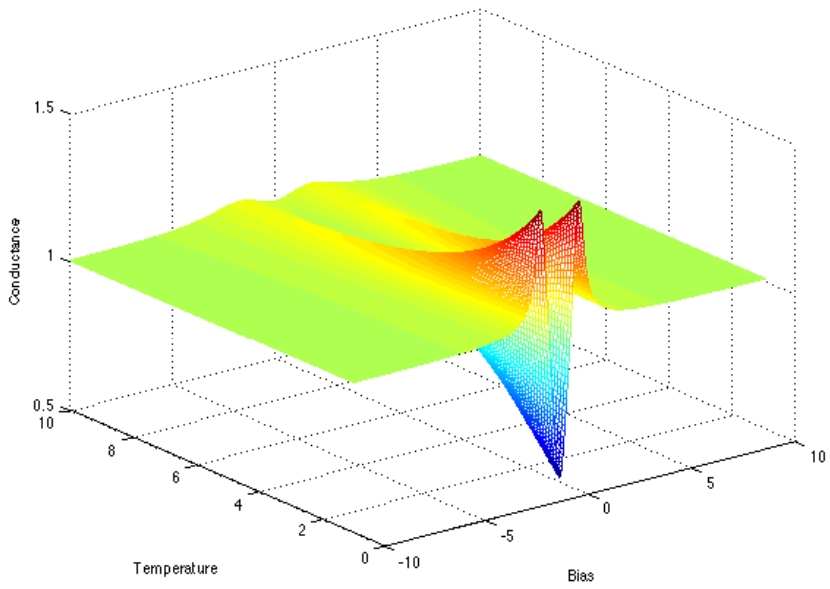

FIGURE 2.8: This figure indicates the relation between temperature, bias and the conductance.The different colours indicate the temperature.

E is "large", we use constant for the point. We define this as calculation (1). Also, we calculate the point values of the derivative of the fermi distribution function at bias zero according to the step length used in the calculation (1). When parameter $E - \mu - eV$ is "large", we make the point value as zero. When We define this as calculation (2). Since calculation (1) and calculation (2) share the same step length, if we need to calculate the differential conductance at a certain bias, we translate the point values of the derivative to that bias and do the integration limited to the non-zero points of the derivative. To avoid lose information, the chosen of the step length is significant. We choose step length according to the smaller peak width between the differential conductance and tunnelling spectroscopy. The method remarkably improves the performance of the calculation yet loses very little accuracy. The weakness of this method is that the computation is slow

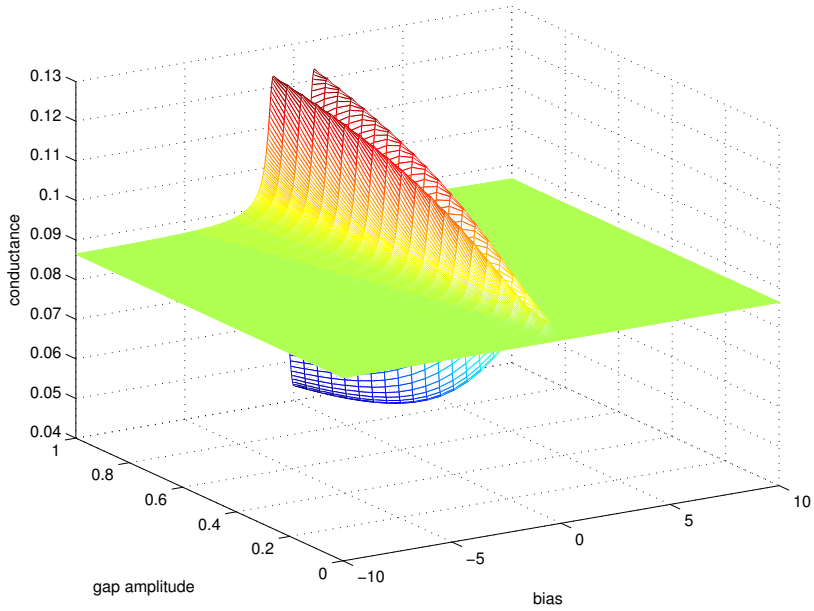

FIGURE 2.9: This figure indicates the relation between energy gap amplitude, bias and the conductance.

when energy gap amplitude is small while the temperature is high, which, however, is easily to be removed by adding some plotting and integrating step boundaries.

2.2.5 c tunnelling spectroscopy and fitting the experimental data

As our experiments are conducted with the materials of c tunnelling of d-wave pair potential, we now focus on this case. The distinction from the ab tunnelling is that the energy gap petal is parallel to the junction interface, leading to the fact that θ in the term (2.23) is the angle in the interface, which we replace the symbol with φ and that we need do an additional integral over φ to complete the solid angle integration; we refer to the formula (2.25) combined with the energy gap (2.23).

The averaged N-I-N junction conductance over the half-sphere of k space could be calculated directly. According to the formula in the following, that calculates the averaged normal conductance,

$$\overline{\sigma_N} = \int_0^{2\pi} d\phi \int_{-\frac{\pi}{2}}^{\frac{\pi}{2}} d\theta \cos\theta \sigma_N \tag{2.26}$$

where we assume that

$$\sigma_N = \frac{1}{1 + (\frac{z}{\cos\theta})^2} \tag{2.27}$$

We could simply calculate the integral for averaged normal conductance,

$$\overline{\sigma_N} = 2\pi\Big(2 - \frac{z^2}{\sqrt{1+z^2}} \ln \frac{\sqrt{1+z^2}+1}{\sqrt{1+z^2}-1}\Big) \tag{2.28}$$

Knowing the formula (2.27), we could skip the numerical integral of normal conductance. Typically the *c* tunnelling spectroscopy is similar to that of *ab* in that they share the same kernel (2.22). That's why it is reasonable even using *s*-wave case to fit the *d*-wave experiments[9]. The following figure shows the comparison with the reference[5].

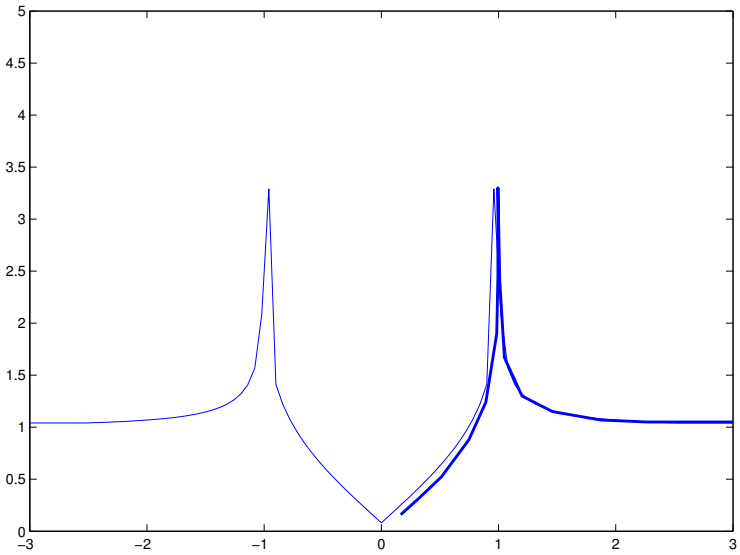

FIGURE 2.10: A simple comparison, where deeper colour represents the digitised data, and $z = 2$

Now we move to fit the data. Fig.2.11 shows the fitting results for our BSCCO on BSC experimental results by manually inputting the parameters.

And chosen energy gaps versus temperature for fitting the experimental data are shown below.

The fitting results are not satisfactory. Only in the dip part the fitting results agree to some extend with the experimental results. But at the both sides they are quite far away. The reason for this disagreement is that the model we use is based on the assumption that the density of states is a constant at (2.15) and the properties of our model is determined by the integration kernel of (2.22), which also has peaks at the point $E = \Delta_0$. The experiment results, however, do not have the corresponding peaks, leading to the fact that the fitting results only match a small part of the experimental results in the centre.

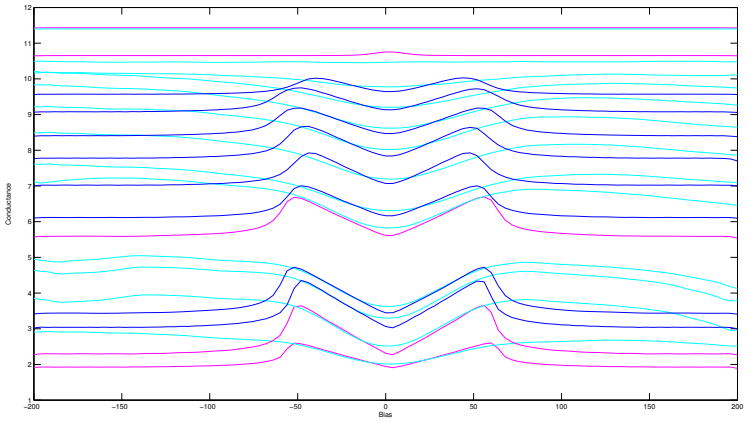

FIGURE 2.11: Conductances normalised by 70K with Temperature, where the deep colour represents calculation. Each bundle represents, from bottom to top, sequentially, $10K$,$13K$,$15K$,$21K$,$30K$,$35K$,$40K$,$45K$,$50K$,$55K$,$65K$,$70K$.

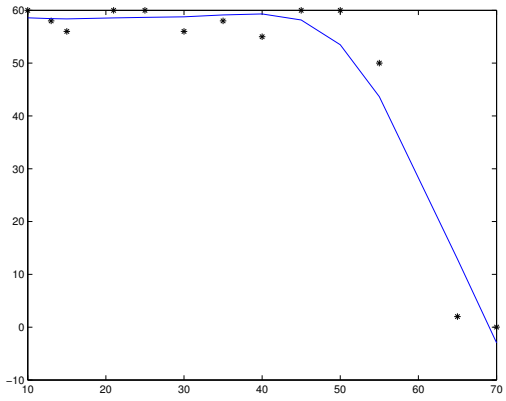

FIGURE 2.12: Energy Gaps with Temperature

To try to eliminate of the disagreement from the computational part, we implemented the genetic algorithm for fitting the data[13].

Genetic algorithm(GA) is an optimisation heuristic inspired by the natural selection process in biological systems. Very similar to the selection process, GA maintains a population of candidates and process mechanisms of encoding, selection, crossover, mutation and culling in the population[13].

In the calculation, we select a population of 50 for the desired parameters randomly generated within the set range and calculate the fitness value, such as standard error and then sort the population according to the fitness value increasingly. Second, we choose the first 25 of the population according to the sorted list as parents while we select another 25 samples of the population as mutants randomly multiplied by some restricted random numbers. 25 selected parents will generate 25 offsprings by crossover.

Then we mix the original population, the generated offspring as well as the 25 mutants together to compose a country of 100 samples. Third, we do sorting again with the population the eliminate the last 50 samples of the population. We will repeat the above three steps until the termination requirement is satisfied.

The above statement is the ideal approach to fit the experimental data, while unfortunately the results come out not satisfactory.

Chapter 3

Tunnelling Spectroscopy with Proximity Effect

Our group currently have a featured paper published containing the topic of proximity effect in d-wave. It is interesting to propose a theory calculating the d-wave conductance accounting for the proximity effect. The work is in progress.

3.1 Bogoliubov Equations

As a matter of fact, the tunnelling conductance discussed in the previous chapter is based on a specific case which is shown in Fig.2.2, where the potential is assumed as a δ function and the pair potential is assumed as a step function, so that Bogoliubov equations(3.1) have an analytical solution, which in contrast, no longer exists when dealing with more complicated case, such as accounting for proximity effect.

3.1.1 Simplification for Bogoliubov Equations

The general Bogoliubov equations are

$$\begin{aligned} i\hbar\frac{\partial f}{\partial t} &= \Big(-\frac{\hbar^2}{2m}\frac{\partial^2}{\partial x^2} - \mu(x) + V(x)\Big) f(x,t) + \Delta(x) g(x,t) \\ i\hbar\frac{\partial g}{\partial t} &= \Big(-\frac{\hbar^2}{2m}\frac{\partial^2}{\partial x^2} - \mu(x) + V(x)\Big) g(x,t) + \Delta(x) f(x,t) \end{aligned} \tag{3.1}$$

(3.1) has the solution form

$$\varphi(x,t) = \begin{pmatrix} f(x,t) \\ g(x,t) \end{pmatrix} \tag{3.2}$$

where $\mu(x), \Delta(x), V(x)$ are chemical potential, energy gap, and the ordinary potential which is related to barrier hight, in which we are interested in the latter two. By introducing a solution of the form

$$\begin{aligned} f &= u(x)e^{ik_F x - \frac{iEt}{\hbar}} \\ g &= v(x)e^{ik_F x - \frac{iEt}{\hbar}} \end{aligned} \tag{3.3}$$

The Bogoliubov equations could be written in this way neglecting higher order terms[10].

$$\begin{aligned} \frac{\partial u}{\partial x} &= i(\pi\xi_0\Delta_\infty)^{-1}[Eu - \Delta(x)v] \\ \frac{\partial v}{\partial x} &= -i(\pi\xi_0\Delta_\infty)^{-1}[Ev - \Delta(x)u] \end{aligned} \tag{3.4}$$

which are the equations we are interested in, ξ_0 is the coherence length.

3.1.2 A Mathematical Approach to Solve the Equation

Various authors have conducted research on solving the Bogoliubov equations[1, 10]. Here we propose a numerical approach method though not implemented to solve the equations. Let the equations (2.4) have the solution form

$$\phi(x) = \begin{pmatrix} u(x) \\ v(x) \end{pmatrix} \tag{3.5}$$

BdG equations could written in a matrix way,

$$\begin{pmatrix} \frac{d}{dz} & 0 \\ 0 & \frac{d}{dz} \end{pmatrix} \phi = \begin{pmatrix} \beta E & 0 \\ 0 & \beta E \end{pmatrix} \phi + \begin{pmatrix} 0 & -\beta\Delta \\ \beta\Delta & 0 \end{pmatrix} \phi \tag{3.6}$$

in other words,

$$D\phi = (I + M)\phi \tag{3.7}$$

We define an newly introduced solution to the following differential equations,

$$D\phi_0 = I\phi_0 \tag{3.8}$$

which can be easily solved,

$$\phi_0 = \begin{pmatrix} e^{\beta Ez} \\ e^{-\beta Ez} \end{pmatrix} \tag{3.9}$$

We set that the final solution by introducing a new matrix, ~~which can be easily solved~~,

$$\phi = P\phi_0 = \begin{pmatrix} p_1 & 0 \\ 0 & p_2 \end{pmatrix} \phi_0 \tag{3.10}$$

We could derive that,

$$D(P\phi_0) = (I + M)(P\phi_0) \tag{3.11}$$

and that,

$$(DP)\phi_0 = (MP)\phi_0 \tag{3.12}$$

Therefore, if we focus on the matrix P, we could reason that,

$$\frac{d}{dz}P = TP \tag{3.13}$$

or

$$\frac{d}{dz}P = \begin{pmatrix} 0 & -\beta\Delta e^{-2\beta Ex} \\ \beta\Delta e^{2\beta Ex} & 0 \end{pmatrix} P \tag{3.14}$$

An approximated way is to compare to the interaction picture,

$$P = \int TP_0 dz + \int T'dz' \int P'TP_0 dz + \cdots \tag{3.15}$$

This method is mathematically clear but computationally confusing. Therefore we didn't implement this method as we have another clear way discussed by the reference[10]

3.1.3 Solving the Bogoliubov Equations

We divide the tunnelling axis into four regions, named 'super','reduced','induced','normal', respectively, which is shown in Fig.3.1, where we already choose parabolic shape for the pair potential. In the 'super' region, the solution has the form of (3.16).

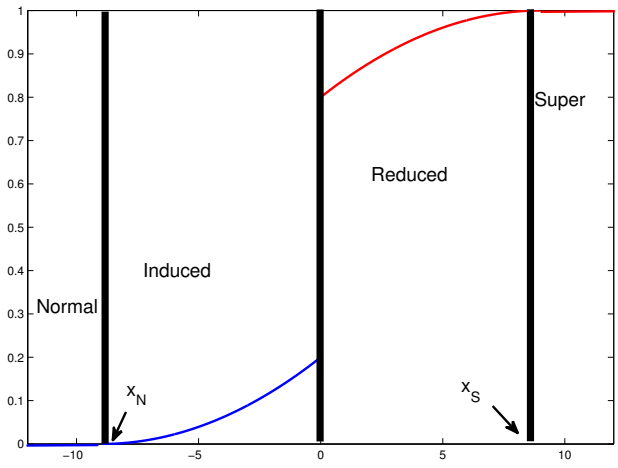

FIGURE 3.1: Parabolic shapes of reduced and induced pair potential. The tunnelling axis is divided into four regions.

$$\varphi_1 = \begin{pmatrix} u_0 \\ v_0 \end{pmatrix} e^{i(k_F+k_S)x}$$
$$\varphi_2 = \begin{pmatrix} v_0 \\ u_0 \end{pmatrix} e^{-i(k_F-k_S)x} \tag{3.16}$$

where parameters are already known,

$$u_0^2 = 1 - v_0^2 = \frac{1}{2}\Big(1 + \frac{(E^2 - \Delta_\infty^2)^{\frac{1}{2}}}{E}\Big) \tag{3.17}$$

and

$$k_S = (E^2 - \Delta_\infty^2)^{1/2}(\pi\xi_0\Delta_\infty)^{-1} \tag{3.18}$$

The solution of this region serves as the generator of boundary conditions for the solution of the next region,'super'.

$$\begin{aligned} u_{a1}(x_S) &= u_{b2}(x_S) = u_0 e^{ik_S x_S} \\ v_{a1}(x_S) &= v_{b2}(x_S) = v_0 e^{ik_S x_S} \\ u_{b1}(x_S) &= u_{a2}(x_S) = 0 \\ u_{b1}(x_S) &= u_{a2}(x_S) = 0 \end{aligned} \tag{3.19}$$

which is for the solution form of the region 'reduced', in which term x_S is described in Fig.3.1, so does term x_N. The solution of reduced region is like (3.20).

$$\varphi_j = \begin{pmatrix} u_{aj} \\ v_{aj} \end{pmatrix} e^{ik_F x} + \begin{pmatrix} u_{bj} \\ v_{bj} \end{pmatrix} e^{-ik_F x}, j = 1, 2 \tag{3.20}$$

After obtaining the numerical solutions for (3.20), we select the values of only one point, which is at $x = 0$

$$\begin{aligned} u_{a1}(0) &= u_{b2}(0) = u_{a1}^{+} \\ v_{a1}(0) &= v_{b2}(0) = v_{a1}^{+} \end{aligned} \tag{3.21}$$

Before we move to the induced region, we make use of the original boundary condition at $x = 0$, setting $V(x) = Z(\pi\xi_0\Delta_\infty)\delta(x)$.

$$\begin{aligned} \varphi^{+} &= \varphi^{-} \\ \frac{\partial\varphi^{+}}{\partial x} - \frac{\partial\varphi^{-}}{\partial x} &= 2k_F Z\varphi^{+} \end{aligned} \tag{3.22}$$

We neglect terms $u_{b1}(x), u_{a2}(x), v_{b1}(x), v_{a2}(x)$as they are zero. We now have the boundary conditions for the induced region

$$\begin{aligned} u_{a0}^{-} &= u_{a1}^{+}, v_{a0}^{-} = v_{a1}^{+} \\ u_{b0}^{-} &= v_{a1}^{+}, v_{b0}^{-} = u_{a1}^{+} \end{aligned} \tag{3.23}$$

And we write the induced region solution form in the following that brings to calculation convenience

$$\varphi_1 = (1+iZ)\begin{pmatrix} u_{a0} \\ v_{a0} \end{pmatrix} e^{ik_F x} - iZ\begin{pmatrix} v_{b0} \\ u_{b0} \end{pmatrix} e^{-ik_F x}$$
$$\varphi_1 = iZ\begin{pmatrix} u_{b0} \\ v_{b0} \end{pmatrix} e^{ik_F x} + (1-iZ)\begin{pmatrix} v_{a0} \\ u_{a0} \end{pmatrix} e^{-ik_F x} \tag{3.24}$$

As a reminder these u, v terms are for numerical calculation who all satisfy the Bogoliubov equations (3.4) while the terms φ are for mathematical analysis.

After the induced solution is numerically obtained, we again choose the value only at $x = -x_N$, which is the interface of induced region and normal region.

$$u_a = u_{a0}(-x_N), v_a = v_{a0}(-x_N)$$
$$u_b = u_{b0}(-x_N), v_b = u_{b0}(-x_N) \tag{3.25}$$

So that the conductance versus energy is written as

$$T = 1 + A - B = 1 + |a_e|^2 - |b_e|^2 \tag{3.26}$$

where,

$$a_e = \frac{(1+Z^2)u_a v_a - Z^2 u_b v_b}{(1+Z^2)u_a^2 - Z^2 u_b^2} e^{-2ik_N x_N}$$
$$a_e = \frac{iZ(1-iZ)(u_b v_a - u_a v_b)}{(1+Z^2)u_a^2 - Z^2 u_b^2} e^{-2ik_N x_N} \tag{3.27}$$

3.2 Analysis of the Solutions of bogoliubov Equations

3.2.1 The Shapes of Reduced and Induced Pair Potential

To be precise we need to compute the pair potential using self-consistent method[14]. Yet we won't lose two much information if we only guess the shape of the pair potential[3, 10]. We are using parabolic shape of pair potential which is like Fig.3.1

Another point we should account for is the proximity thickness, which will affect much the shape of the computed results. We define

$$x_S = a_S \pi \xi_0, x_N = a_N \pi \xi_0 \tag{3.28}$$

where in effect we find only the factors a_S, a_N play the role of influencing the results. Therefore, we choose the potential function as

$$\begin{aligned} \Delta_R &= \frac{\Delta_+ - \Delta_\infty}{x_S^2}(x - x_S)^2 + \Delta_\infty \\ \Delta_I &= \frac{\Delta_-}{x_N^2}(x + x_S)^2 \end{aligned} \tag{3.29}$$

who have the shapes in Fig.3.1. Now let us first study some intermediate values in the calculation.

3.2.2 Shapes of $|u|, |v|$

We take a look at the shapes of $|u|, |v|$, which are also affected by the chosen energy value E and if not noted, the bulk potential is always set to $\Delta_\infty = 1$

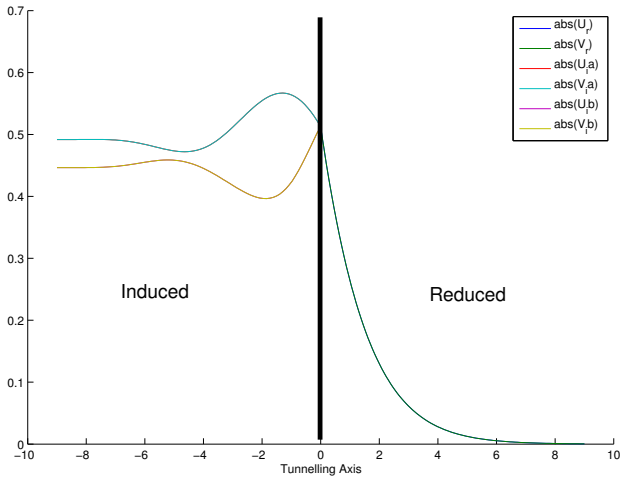

FIGURE 3.2: The shapes with $E = 0.5$, subscript r indicates reduced region while i induced region. Notice that in reduced region, $u^* = v$.

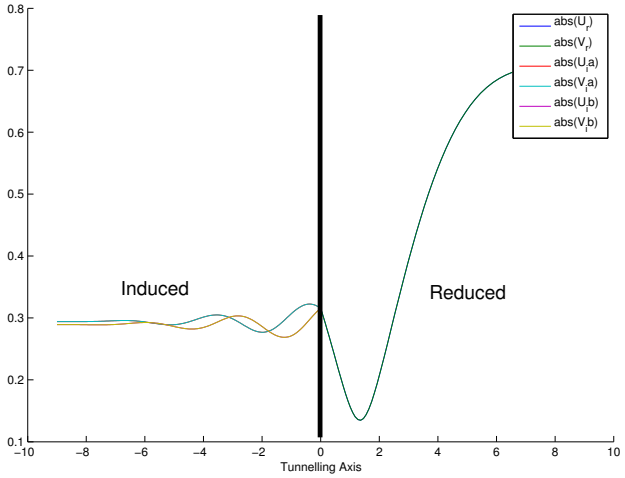

FIGURE 3.3: The shapes with $E = 1$, subscript r indicates reduced region while i induced region

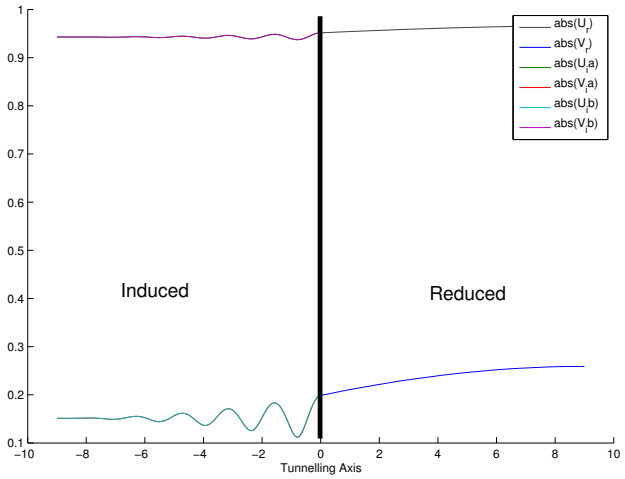

FIGURE 3.4: The shapes with $E = 2$, subscript r indicates reduced region while i induced region

3.2.3 The Specific Case of BTK

First of all we check the reliability of our model. Ideally, BTK is a specific case of our discussion in this chapter; in other words, if we set $\Delta_R = 1, \Delta_I = 0$, we should see the results of BTK, Fig3.5. Here are a set of figures, in which the deep blue one represents the BTK, the famous V-shape shown. Also, when barrier hight $Z = 0$, we should observe flat region with the value of 2 in the middle, Fig.3.6.

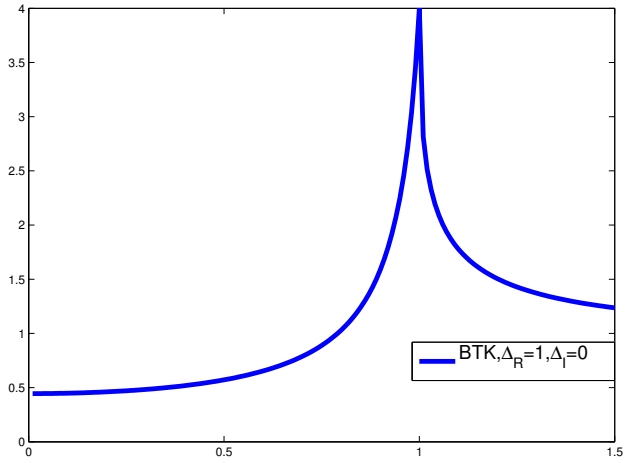

FIGURE 3.5: BTK case when we set $\Delta_R = 1, \Delta_I = 0$

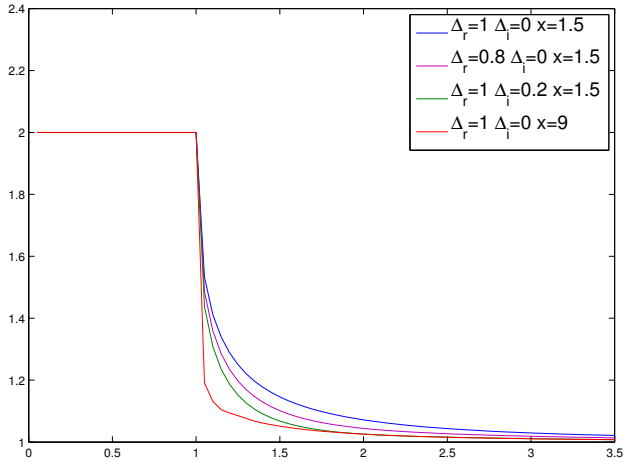

FIGURE 3.6: The flat region in the middle appears no matter what parameters we set

3.3 Tunnelling Spectroscopy with Proximity Effect

Similar to the procedure in the previous chapter, with solutions obtained, we first have a look at the kernel of the conductance.

$$\sigma_T = 1 + A - B \tag{3.30}$$

3.3.1 Proximity Effect with various parameters

We draw a list of figures showing the change of the shape according to the varying reduced gap and induced gap, setting the coherence length as $\pi\xi_0 = 1$, Fig.3.7, Fig.3.8. In addition, we plot another group of figures with $Z = 0.3$, Fig.3.10-Fig.3.13.

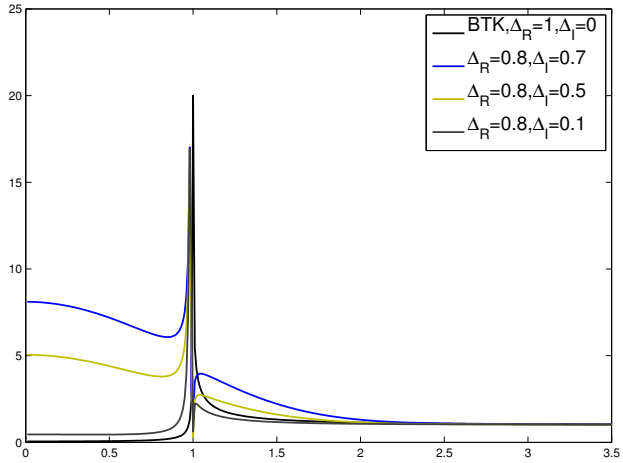

FIGURE 3.7: The figure indicates the difference with induced gap varying.$Z = 3$.

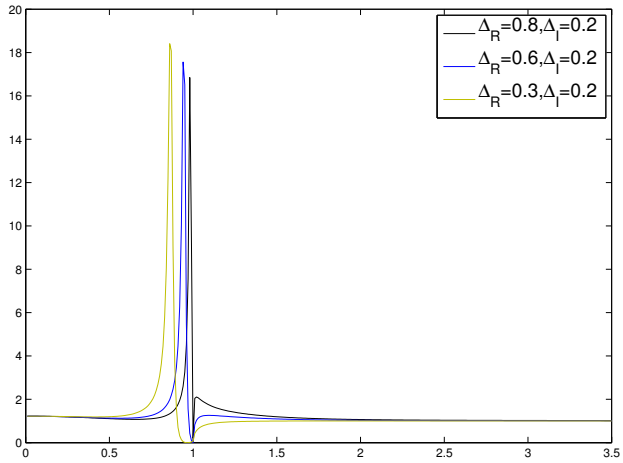

FIGURE 3.8: The figure indicates the difference with reduced gap varying.$Z = 3$

As a thought, the proximity domain certainly affects the behaviours of the transmission. Here I did research on the influences. Fig.3.9 indicates the relationship between proximity domain and the shape of the conductance, with reduced gap 0.8 and induced gap 0.4.

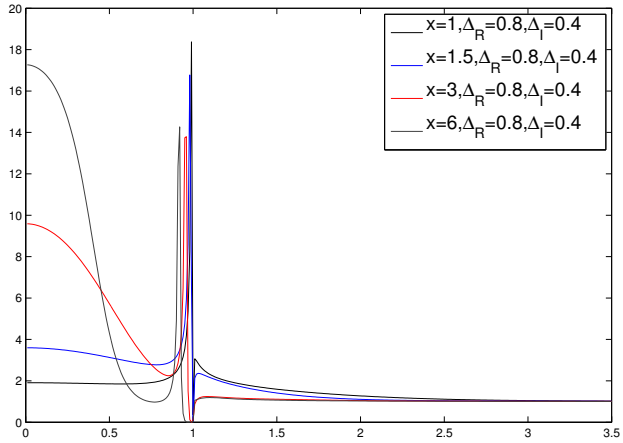

FIGURE 3.9: The proximity domains affects the left side of the shape significant y.$Z = 3$

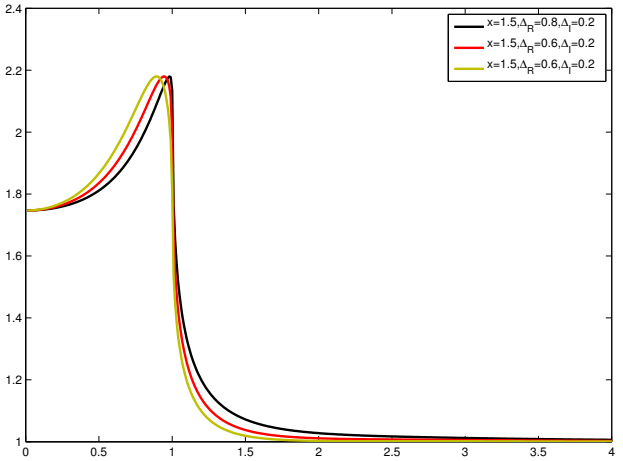

FIGURE 3.10: Low barrier hight.$Z = 0.3$

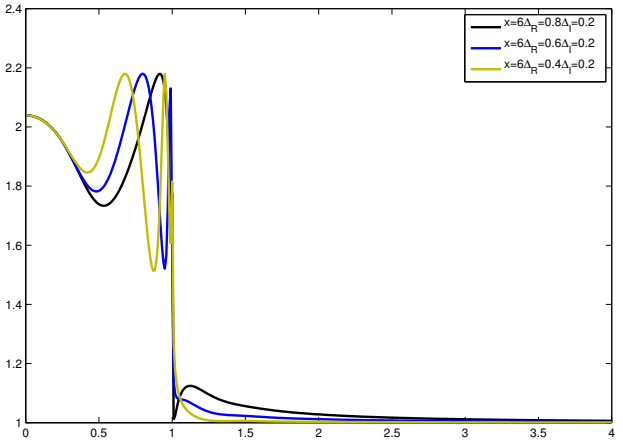

FIGURE 3.11: Some peaks show if thicker proximity domain is chosen at low barrier hight.$Z = 0.3$

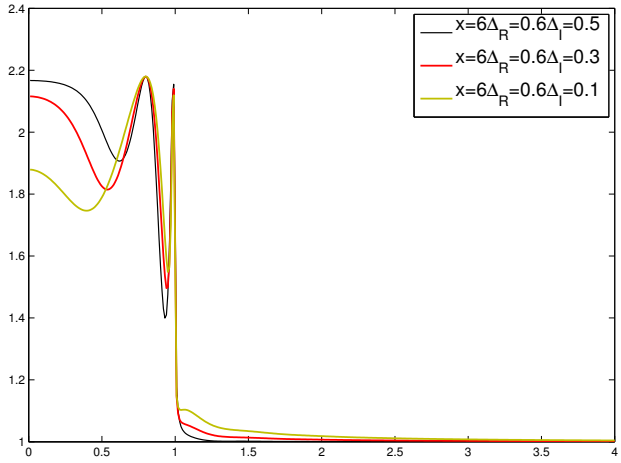

FIGURE 3.12: Some peaks show if thicker proximity domain is chosen at low barrier hight.$Z = 0.3$

We set the proximity effect parameters as $x_S = x_N = 9, Z = 0.3$, we obtain the Fig.3.16. Their physical meanings, however, remains to be discovered. In this figure, we obtained a number of peaks.

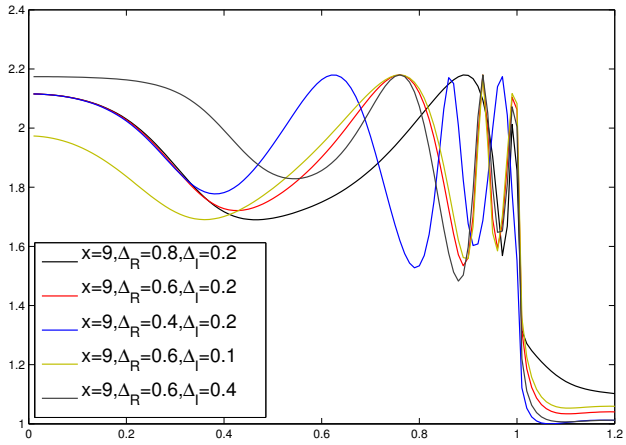

FIGURE 3.13: Some peaks show if thicker proximity domain is chosen at low barrier hight.$Z = 0.3$

3.3.2 *s* wave tunnelling spectroscopy with proximity effect

The induced gap brings a bulk in the middle intead of the desired peaks and the function of reduced gap remains unknown. Here we make a small trial step moving to *s* tunnelling spectroscopy, whose shapes though look like those of un-integrated ones. In Fig.3.13,

we could see the effects of induced gap. The induced gap creates a bulk in the middle.

$$\sigma_T(E) = \frac{\int_0^{2\pi} d\varphi \int_{-\frac{\pi}{2}}^{\frac{\pi}{2}} d\theta \sigma_S(E) \cos\theta}{\int_0^{2\pi} d\varphi \int_{-\frac{\pi}{2}}^{\frac{\pi}{2}} d\theta \sigma_N \cos\theta} \tag{3.31}$$

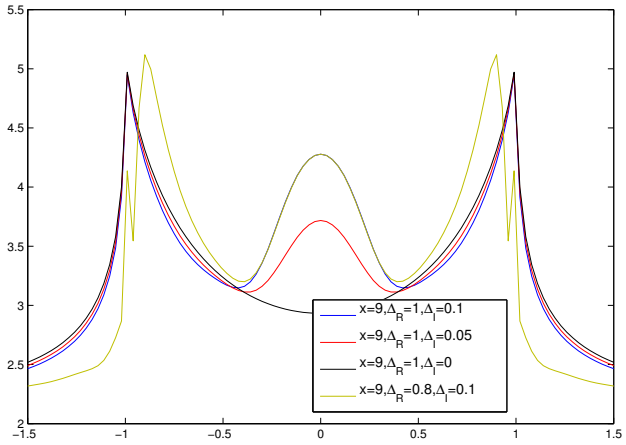

FIGURE 3.14: The *s*-wave tunnelling spectroscopy. The induced gap creates a bulk in the middle of the figure

I thought you did d-wave? Where is it?

Chapter 4

Future Work

We concludes our work of calculating d-wave tunnelling spectroscopy and fitting the experimental data as well as the calculation the tunnelling spectroscopy accounting for proximity effect.

For the work described in Chapter 2, first of all we need to modify our model. As stated at the end of Chapter 2, the density of states is assumed to be constant, which might probably not be true. Also, we need to perform a calculation using genetic algorithm which is more reliable.

For the work calculating the proximity effect, though it reproduces quite well for the spercfic known cases in Fig.3.5,Fig.3.6, the picture of reduced gap and induced gap is blurred; we do not have a clear idea of what their effects are. Moreover, it seems that our calculated results do not agree with the experimental results well albeit we just reach the s-wave tunnelling conductance calculation. Only if these blocks are cleared can we move forward to our d-wave proximity tunnelling conductance calculation.

Chapter 5

Additional Projects

5.1 Control System for Raman Stage and Fresnel Rhomb

The software I designed integrates the XYZ stage control panel and the Fresnel Rhomb control panel. Users can operate XYZ stage and the Fresnel Rhomb at the same time with convenience. For XYZ stage control part, apart from controlling the stage, users can store the positions of their samples that may be studied later. For Fresnel control part, the digits shown on the software are really polarization angles so that users do not need to convert the units. In addition, a polarization clock is provided to assist the operation. What is more, the COM interface is also adjustable even in the case that the software is installed in a substituted computer.

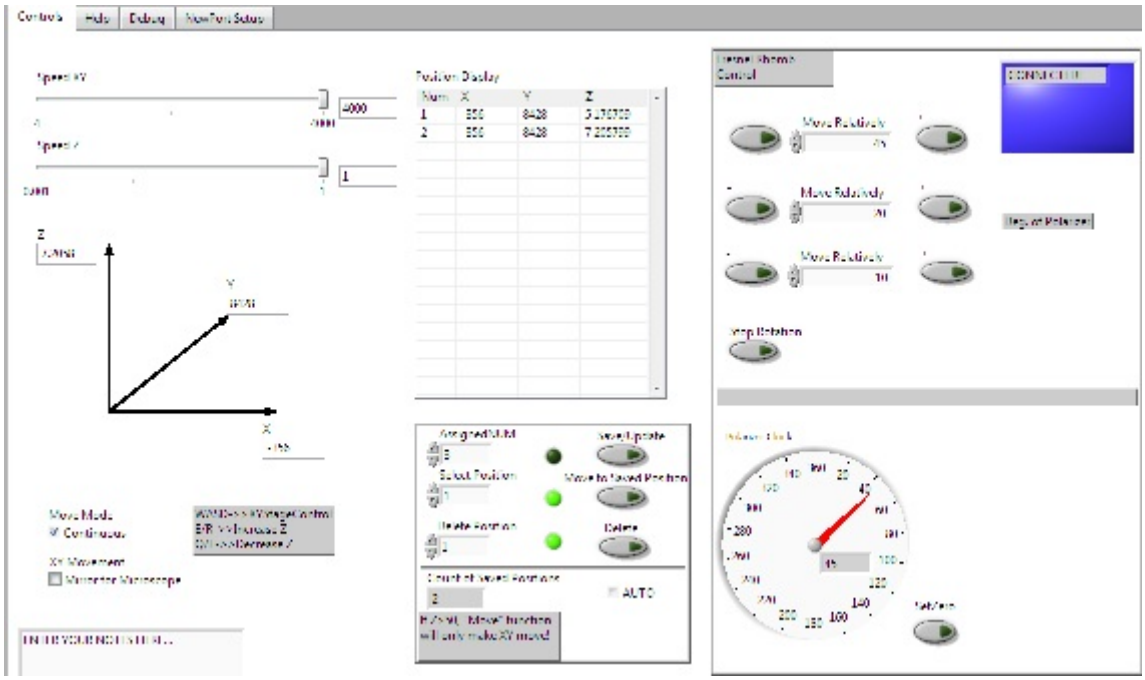

FIGURE 5.1: Main Control Panel

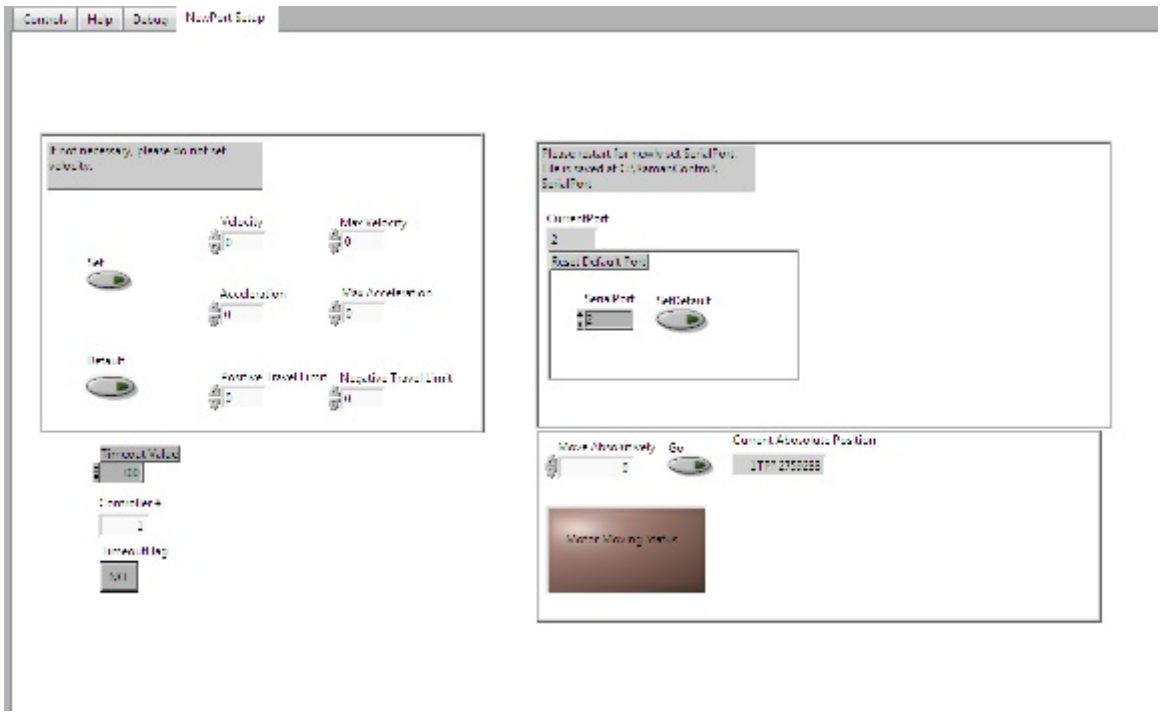

FIGURE 5.2: Setup Control Panel

Bibliography

[1] G. E. Blonder, M. Tinkham, and T. M. Klapwijk. Transition from metallic to tunneling regimes in superconducting microconstrictions: Excess current, charge imbalance, and supercurrent conversion. *Phys. Rev. B*, 25:4515–4532, Apr 1982. doi: 10.1103/PhysRevB.25.4515. URL http://link.aps.org/doi/10.1103/PhysRevB.25.4515.

[2] S. Guéron, H. Pothier, Norman O. Birge, D. Esteve, and M. H. Devoret. Superconducting proximity effect probed on a mesoscopic length scale. *Phys. Rev. Lett.*, 77:3025–3028, Sep 1996. doi: 10.1103/PhysRevLett.77.3025. URL http://link.aps.org/doi/10.1103/PhysRevLett.77.3025.

[3] D. R. Heslinga, S. E. Shafranjuk, H. van Kempen, and T. M. Klapwijk. Observation of double-gap-edge andreev reflection at si/nb interfaces by point-contact spectroscopy. *Phys. Rev. B*, 49:10484–10494, Apr 1994. doi: 10.1103/PhysRevB.49.10484. URL http://link.aps.org/doi/10.1103/PhysRevB.49.10484.

[4] S. Guéron, H. Pothier, Norman O. Birge, D. Esteve, and M. H. Devoret. Superconducting proximity effect probed on a mesoscopic length scale. *Phys. Rev. Lett.*, 77:3025–3028, Sep 1996. doi: 10.1103/PhysRevLett.77.3025. URL http://link.aps.org/doi/10.1103/PhysRevLett.77.3025.

[5] Satoshi Kashiwaya, Yukio Tanaka, Masao Koyanagi, and Koji Kajimura. Theory for tunneling spectroscopy of anisotropic superconductors. *Phys. Rev. B*, 53:2667–2676, Feb 1996. doi: 10.1103/PhysRevB.53.2667. URL http://link.aps.org/doi/10.1103/PhysRevB.53.2667.

[6] Yukio Tanaka and Satoshi Kashiwaya. Theory of tunneling spectroscopy of *d*-wave superconductors. *Phys. Rev. Lett.*, 74:3451–3454, Apr 1995. doi: 10.1103/PhysRevLett.74.3451. URL http://link.aps.org/doi/10.1103/PhysRevLett.74.3451.

[7] Yukio Tanaka and Satoshi Kashiwaya. Theory of tunneling spectroscopy of *d*-wave superconductors. *Phys. Rev. Lett.*, 74:3451–3454, Apr 1995. doi: 10.1103/

PhysRevLett.74.3451. URL http://link.aps.org/doi/10.1103/PhysRevLett.74.3451.

[8] Oded Millo, Itay Asulin, Ofer Yuli, Israel Felner, Zhi-An Ren, Xiao-Li Shen, Guang-Can Che, and Zhong-Xian Zhao. Scanning tunneling spectroscopy of $smfeaso_{0.85}$: Possible evidence for *d*-wave order-parameter symmetry. *Phys. Rev. B*, 78:092505, Sep 2008. doi: 10.1103/PhysRevB.78.092505. URL http://link.aps.org/doi/10.1103/PhysRevB.78.092505.

[9] W. K. Park, L. H. Greene, J. L. Sarrao, and J. D. Thompson. Andreev reflection at the normal-metal/heavy-fermion superconductor $CeCoin_5$ interface. *Phys. Rev. B*, 72:052509, Aug 2005. doi: 10.1103/PhysRevB.72.052509. URL http://link.aps.org/doi/10.1103/PhysRevB.72.052509.

[10] P. C. van Son, H. van Kempen, and P. Wyder. Andreev reflection and geometrical resonance effects for a gradual variation of the pair potential near the normal-metal ˘ superconductor interface. *Phys. Rev. B*, 37:5015–5023, Apr 1988. doi: 10.1103/PhysRevB.37.5015. URL http://link.aps.org/doi/10.1103/PhysRevB.37.5015.

[11] Chr. Bruder. Andreev scattering in anisotropic superconductors. *Phys. Rev. B*, 41: 4017–4032, Mar 1990. doi: 10.1103/PhysRevB.41.4017. URL http://link.aps.org/doi/10.1103/PhysRevB.41.4017.

[12] J. Bardeen, L. N. Cooper, and J. R. Schrieffer. Theory of superconductivity. *Phys. Rev.*, 108:1175–1204, Dec 1957. doi: 10.1103/PhysRev.108.1175. URL http://link.aps.org/doi/10.1103/PhysRev.108.1175.

[13] A.E Smith M.Gulsen and D.M. Tale. A genetic algorithm approach to curve fitting. *INT. J. PROD. RES*, 33:1911–1923, July 1995. doi: 10.1080/00207549508904789. URL http://www.tandfonline.com/doi/abs/10.1080/00207549508904789.

[14] Chr. Bruder. Andreev scattering in anisotropic superconductors. *Phys. Rev. B*, 41: 4017–4032, Mar 1990. doi: 10.1103/PhysRevB.41.4017. URL http://link.aps.org/doi/10.1103/PhysRevB.41.4017.